

Supplemental Material for
Helical motors and formins synergize to compact chiral filopodial
bundles:
Mathematical and computational models and supplementary figures

Ondrej Maxian^{1,3,4} and Alex Mogilner^{1,2,*}

¹*Courant Institute, New York University, New York, NY 10012, USA*

²*Department of Biology, New York University, New York, NY 10012, USA*

³*Department of Molecular Genetics and Cell Biology, University of Chicago, Chicago, IL 60615, USA*

⁴*Institute for Biophysical Dynamics, University of Chicago, Chicago, IL 60615, USA*

1 Mathematical model of actin filaments and forces

In this work, we model actin filaments as inextensible Euler beams which are subject to bending and twisting forces. The numerical method we choose is based on previous work by some of us [18], which developed a spectral discretization for such filaments. In this section, we summarize our previous work and highlight a few small changes.

We let $\mathbb{X}(s)$ be a parameterization of the filament centerline, and introduce an operator $\mathcal{K}[\mathbb{X}(\cdot)]$ which parameterizes the space of inextensible filament motions. The translational velocity can be written in terms of such motions as

$$\mathbf{U}(s) = \mathbf{U}_{\text{MP}} + \int_{L/2}^s (\boldsymbol{\Omega}(s') \times \boldsymbol{\tau}(s')) ds' := (\mathcal{K}[\mathbb{X}(\cdot)] \boldsymbol{\alpha})(s) \quad (\text{S1})$$

where \mathbf{U}_{MP} is the velocity of the filament midpoint and $\boldsymbol{\alpha} = (\boldsymbol{\Omega}, \mathbf{U}_{\text{MP}})$ represents the translational degrees of freedom. In continuum, the dynamics of the centerline are then governed by the saddle-

point system

$$\begin{pmatrix} -\mathcal{M}_{\text{tt}} & \mathcal{K} \\ \mathcal{K}^* & \mathbf{0} \end{pmatrix} \begin{pmatrix} \boldsymbol{\lambda} \\ \boldsymbol{\alpha} \end{pmatrix} = \begin{pmatrix} \mathcal{M}_{\text{tt}} \left(\mathbf{f}^{(\kappa)} + \mathbf{f}^{(\gamma)} + \mathbf{f}^{(\text{ext})} \right) \\ \mathbf{0} \end{pmatrix}, \quad (\text{S2})$$

$$\text{where } \mathbf{f}^{(\kappa)} = -\kappa \partial_s^4 \mathbb{X}, \quad \mathbf{f}^{(\gamma)} = \gamma \partial_s \left(\psi \left(\partial_s \mathbb{X} \times \partial_s^2 \mathbb{X} \right) \right).$$

The first equation says that the total velocity is obtained by multiplying the total force density, which is composed of the constraint force $\boldsymbol{\lambda}$, the bending force $\mathbf{f}^{(\kappa)}$, the twisting force $\mathbf{f}^{(\gamma)}$, and any external forcing $\mathbf{f}^{(\text{ext})}$, by the mobility \mathcal{M}_{tt} . The twisting force $\mathbf{f}^{(\gamma)}$ is related to the fiber position \mathbb{X} and the twist density $\psi = \partial_s \theta$, where $\theta(s)$ is the angle of twist of the cross-sectional material frame relative to the twist-free Bishop frame [2]. Here, for simplicity, we have also neglected the so-called rotation-translation and translation-rotation mobilities [18], which take into account the translational velocity induced by torque and rotational velocity induced by force, so that we only couple twist to translation through the twist force $\mathbf{f}^{(\gamma)}$, similar to other studies of rod mechanics [31, 12]. The second equation in (S2), $\mathcal{K}^* \boldsymbol{\lambda} = \mathbf{0}$, enforces the principle of virtual work, which says that the constraint forces $\boldsymbol{\lambda}$ perform no work with respect to all inextensible motions. As discussed in [18, Sec. III(A)], this constraint is equivalent to setting $\boldsymbol{\lambda} = \partial_s (T \boldsymbol{\tau})$, for some line tension $T(s)$ [27].

The twist density on the filament centerline evolves via an auxiliary set of equations. The total parallel torque is given by

$$n^{\parallel} = \gamma \partial_s \psi + n^{(\text{ext})}, \quad (\text{S3})$$

where the first term is the parallel torque due to twisting, and the second one represents externally-applied torques (e.g., from motors or crosslinkers). The twist-density ψ then evolves according to the equation

$$\partial_t \psi = \partial_s \Omega^{\parallel} - (\boldsymbol{\Omega} \cdot \partial_s \boldsymbol{\tau}) = \partial_s \Omega^{\parallel} - \left(\boldsymbol{\Omega}^{\perp} \cdot \partial_s \boldsymbol{\tau} \right) \quad (\text{S4})$$

$$\text{where } \Omega^{\parallel} = m_{\text{tr}} \left(n^{\parallel} \boldsymbol{\tau} \right) \cdot \boldsymbol{\tau}, \quad (\text{S5})$$

is the parallel rate of rotation, the perpendicular rate $\boldsymbol{\Omega}$ is obtained from the solution of (S2), and m_{tr} represents the mobility (inverse of drag) relationship between (parallel) torque and (parallel) angular velocity.

Our simulations use a clamped end at the filopodium base ($s = 0$),

$$\mathbb{X}(s = 0) = \mathbf{X}_0, \quad \partial_s \mathbb{X}(s = 0) = \boldsymbol{\tau}_0, \quad \Omega^{\parallel}(s = 0) = 0, \quad (\text{S6})$$

where \mathbf{X}_0 and $\boldsymbol{\tau}_0$ are the fixed endpoint position and tangent vector, respectively. At the clamped end, we assume that the parallel angular velocity is zero,

$$\Omega^\parallel(s=0) = m_{\text{rr}}\gamma\partial_s\psi(0) = 0 \rightarrow \partial_s\psi(0) = 0. \quad (\text{S7})$$

The $s = L$ is more delicate. There, we assume that a clamped formin exerts a fixed *torque* N_L on the fiber,

$$N_L = \gamma\psi(L) \rightarrow \psi(L) = N_L/\gamma, \quad (\text{S8})$$

while the position of the fiber end is free,

$$\partial_s^2\mathbb{X}(s=L) = \mathbf{0}, \quad \partial_s^3\mathbb{X}(s=L) = \mathbf{0}. \quad (\text{S9})$$

Based on (S8), we see that our fixed torque BC is equivalent to formin exerting a fixed twist at the $s = L$ end that is constant in time. At steady state (see Section 2), this corresponds to a constant twist along the fiber, or a constant rotation of the cross section per unit length. Since the twist per unit length is constant, adding length via polymerization then increases the twist angle at the plus (formin-bound) end, meaning that monomers are added at a fixed angle of twist without affecting the rest of the filament [25, 10]. An alternative boundary condition is to assume that formin exerts a fixed *angular velocity* on the $s = L$ end, in which case $\partial_s\psi(L) \equiv \psi_L$. This boundary condition gives no steady state and only specifies twist up to a constant, i.e., it only specifies rotation up to an unknown angle per unit length. For this reason, we reject it as unphysical.

In this work, we are interested in capturing the qualitative behavior of the filaments, but not necessarily the quantitative hydrodynamics. Because of that, we will neglect all hydrodynamic interactions between filaments (and between far-away parts of a single filament), and any coupling between rotation and translation. For the purposes of this study, we only want to capture the qualitative separation of scales between bending and twisting. Because of this, we use the local drag mobilities [22]

$$\boldsymbol{\mathcal{M}}_{\text{tt}}(s) = \frac{\ln(\epsilon^{-2})}{8\pi\mu} \left(\mathbf{I} + \widehat{\partial_s\mathbb{X}}(s)\widehat{\partial_s\mathbb{X}}(s) \right), \quad m_{\text{rr}} = \frac{1}{4\pi\mu a^2}, \quad (\text{S10})$$

where a is the filament radius and $\epsilon(t) = a/L(t)$ is the filament aspect ratio. Here the translational mobility $\boldsymbol{\mathcal{M}}_{\text{tt}}$ is a 3×3 matrix on each filament point, which expresses the fact that the resistance in the tangential direction is half that in the perpendicular direction. The rotational mobility m_{rr} is a scalar that relates parallel torque n^\parallel to rotational velocity Ω^\parallel . These mobilities are the minimal number of quantities necessary to capture the separation of scales (twist equilibrates $\mathcal{O}(\epsilon^{-2})$ -fold faster than force).

Because all quantities are ultimately discrete in simulations, we discretize the continuum curve $\mathbb{X}(s)$ using a set of N_x Chebyshev nodes, which we denote by \mathbf{X} . These nodes define an interpolating function, which can be used at any point to obtain the position $\mathbb{X}(s)$ (see [17, Sec. 1] or [13, Sec. 6.1] for an explanation of our discretization). Once we have a spatial discretization, the saddle point system (S2) becomes a discrete matrix equation that we solve at each time step. To make our time-marching scheme stable for larger time steps, we treat the bending force implicitly; see [13, Sec. 6.4] for more details.

1.1 Crosslinking

To compute crosslinking forces between pairs of filaments, we use the methodology described in [17, Sec. 6] to transform forces on a grid of uniformly spaced points along the filaments to forces on the Chebyshev grid. The forces can then be converted to the force density $\mathbf{f}^{(\text{CL})}$ by multiplying by an inverse weights matrix.

For the uniform points, we resample the filament $\mathbb{X}(s)$ at N_u uniformly-spaced locations, obtaining a vector $\bar{\mathbf{X}}$ of sites where crosslinks are bound. The relationship between the two is given by

$$\bar{\mathbf{X}} = \mathbf{R}^{(u)} \mathbf{X} \leftrightarrow \bar{\mathbf{X}}_{\{p\}} = \mathbf{R}_{\{p,: \}}^{(u)} \mathbf{X}, \quad (\text{S11})$$

where $\mathbf{R}^{(u)}$ is the resampling matrix and $\mathbf{R}_{\{p,: \}}^{(u)}$ is its p th row.

Denoting the uniform points connected by the crosslink with $\bar{\mathbf{X}}_{\{p\}}^{(i)}$ and $\bar{\mathbf{X}}_{\{q\}}^{(j)}$, we have the displacement

$$\mathbf{r} = \bar{\mathbf{X}}_{\{p\}}^{(i)} - \bar{\mathbf{X}}_{\{q\}}^{(j)} = \mathbf{R}_{\{p,: \}}^{(u)} \mathbf{X}^{(i)} - \mathbf{R}_{\{q,: \}}^{(u)} \mathbf{X}^{(j)} \quad (\text{S12})$$

with $r = \|\mathbf{r}\|$. Then, let us postulate the crosslink energy and force,

$$\mathcal{E}(r) = \frac{K_c}{2} (r - \ell_c)^2 \quad (\text{S13})$$

$$\frac{\partial \mathcal{E}}{\partial r} = K_c (r - \ell_c), \quad (\text{S14})$$

respectively, between the two uniform points, where K_c is the spring constant for the crosslink (units force/length) and ℓ_c is the rest length. The corresponding force on filaments i and j can then be obtained by differentiating the energy

$$\begin{aligned} \mathbf{F}_{\{a\}}^{(i)} &= -\frac{\partial \mathcal{E}}{\partial r} \frac{\partial r}{\partial \mathbf{X}_{\{a\}}^{(i)}} & \mathbf{F}_{\{b\}}^{(j)} &= -\frac{\partial \mathcal{E}}{\partial r} \frac{\partial r}{\partial \mathbf{X}_{\{b\}}^{(j)}} \\ \mathbf{F}_{\{a\}}^{(i)} &= -\frac{\partial \mathcal{E}}{\partial r} \hat{\mathbf{r}} \mathbf{R}_{\{p,a\}}^{(u)} & \mathbf{F}_{\{b\}}^{(j)} &= \frac{\partial \mathcal{E}}{\partial r} \hat{\mathbf{r}} \mathbf{R}_{\{q,b\}}^{(u)}. \end{aligned} \quad (\text{S15})$$

Note that in the energy (S13), the crosslinks are linear springs that connect to the filaments by flexible joints, so possible bending forces are ignored. Also, the crosslinks bind, effectively, to the 1D contour of a filament, so potential effects from the specific distribution of binding sites along the helical grooves of the filaments are also ignored.

1.1.1 Dynamic crosslinks

To implement dynamic crosslinking, we use a simplified version of the algorithm described in [16]. Each filament is discretized into $N_u = 41$ binding sites. We assume that crosslinkers have rest length ℓ_c , and can stretch at most by a length $\Delta\ell = 2\sqrt{k_B T/K_c}$. Thus, at each time step, we find all pairs of uniform sites on distinct fibers separated by a distance between $\ell_c - \Delta\ell$ and $\ell_c + \Delta\ell$, and assign to each pair a binding rate k_{on} in units of 1/s.¹ We also assign each already bound link an unbinding rate of k_{off} . This gives a set of reactions and rates, which we simulate at each time step using Gillespie's next reaction method [1, 5]. To simplify the algorithm, we assume that unbound links will not rebind in a single time step, and that bound links will not unbind in a single time step. Our previous work had a more detailed model where each end of a crosslinker is distinct; here we simply treat the crosslink as one entity that is bound or unbound.

1.2 Steric forces

We compute steric interaction forces using the method described in [14, Sec. 9.2]. In brief, the steric interaction energy between filaments i and j can be written as

$$\begin{aligned}\mathcal{E}^{(ij)} &= \int_0^L \int_0^L \hat{\mathcal{E}}\left(r\left(s^{(i)}, s^{(j)}\right)\right) ds^{(i)} ds^{(j)}, \\ r\left(s^{(i)}, s^{(j)}\right) &= \left\| \mathbb{X}^{(i)}\left(s^{(i)}\right) - \mathbb{X}^{(j)}\left(s^{(j)}\right) \right\|,\end{aligned}\tag{S16}$$

where $\hat{\mathcal{E}}$ is the potential density function

$$\begin{aligned}\hat{\mathcal{E}}(r) &= \frac{\mathcal{E}_0}{a^2} \text{erf}\left(r/(\delta\sqrt{2})\right) \\ \frac{d\hat{\mathcal{E}}}{dr} &= \frac{\mathcal{E}_0}{a^2\delta} \sqrt{\frac{2}{\pi}} \exp\left(-r^2/(2\delta^2)\right),\end{aligned}\tag{S17}$$

where the Gaussian is truncated at $r_{\text{max}} = 4\delta$, and $\mathcal{E}_0 = 4k_B T$ [26] is the magnitude of the steric force, which leaves $\delta = a$ is the parameter that controls the Gaussian decay.

¹Technically, the CL on rate should have units of 1/(length×time) to be discretization independent. This is actually complex when the filament length changes in time, so we simply choose a value that gives a characteristic number of engaged crosslinks for a given discretization.

To determine the forces, we compute the double integral (S16) for energy via upsampling the position to a high-resolution Chebyshev grid, then differentiate to get force. Similar to the cross-linking force, we denote the upsampled points via $\bar{\mathbf{X}} = \mathbf{E}\mathbf{X}$. The double integral can then be evaluated and differentiated via

$$\mathcal{E} = \sum_k \sum_j \hat{\mathcal{E}} \left(\left\| \bar{\mathbf{X}}_{\{k\}} - \bar{\mathbf{X}}_{\{j\}} \right\| \right) w_k w_j \quad (\text{S18})$$

$$\begin{aligned} &= \sum_k \sum_j \hat{\mathcal{E}} \left(\left\| \mathbf{E}_{kp} \mathbf{X}_{\{p\}} - \mathbf{E}_{jq} \mathbf{X}_{\{q\}} \right\| \right) w_k w_j \\ \mathbf{F}_{\{a\}}^{(i)} &= -\frac{\partial \mathcal{E}}{\partial \mathbf{X}_{\{a\}}^{(i)}} = -\sum_k \sum_j \frac{\partial \hat{\mathcal{E}}}{\partial r} (r_{kj}) \hat{\mathbf{r}}_{kj} \mathbf{E}_{ka} w_k w_j. \end{aligned} \quad (\text{S19})$$

The last equation gives the force at Chebyshev node a on filament i , and is a function of the integration weights w_k and w_j of points k and j on the upsampled grid. In this work, we use $N_u = 101$ upsampling points to compute the steric forces on the filaments, and the points we choose are at arclength coordinates $s = 0, \Delta s_u, \dots, L$, where $\Delta s_u = L/(N_u - 1)$ is the spacing. The corresponding weights are $w = \Delta s_u/2, \Delta s_u, \dots, \Delta s_u, \Delta s_u/2$, so that the first and last point have a weight of $1/2$, in accordance with the trapezoid rule. Note that the sum (S19) can be computed efficiently via a neighbor search (`rangesearch` in Matlab).

1.3 Numerical method for polymerization

To model linear polymerization of a filament $\mathbb{X}(s)$ at the $s = L$ end, we use the following algorithm:

1. Sample the Chebyshev interpolants $\mathbb{X}(s = L)$ and $\partial_s \mathbb{X}(s = L)$ to obtain the position and tangent vector at $s = L$. Let \mathbf{X}_L denote the position and $\boldsymbol{\tau}_L$ denote the normalized tangent vector.
2. Add an additional point to the matrix of Chebyshev nodes,

$$\widetilde{\mathbf{X}} = \begin{pmatrix} \mathbf{X} \\ \mathbf{X}_L + L'(t)\Delta t \boldsymbol{\tau}_L \end{pmatrix}. \quad (\text{S20})$$

3. Reparameterize the filament by its new length. That is, the new set of evaluation points in s is given by $\tilde{\mathbf{s}} = (\mathbf{s}, L + L'(t)\Delta t) / (L + L'(t)\Delta t)$ and goes from zero to one.
4. Let \mathbf{R} be the matrix that evaluates the Chebyshev interpolant defined by the arclength points \mathbf{s} at $\tilde{\mathbf{s}}$. Then set $\mathbf{X} = \mathbf{R}^\dagger \widetilde{\mathbf{X}}$ to obtain the positions at the Chebyshev nodes at the next time step. This resamples the filament at the nodes \mathbf{s} , but in the new parameterization.

5. The parameter s is no longer an arclength parameter, but is the distance in *reference arclength* coordinates. The new arclength parameter is given by

$$s^*(s, t) = L(t)/L(0)s.$$

Thus, at the next time step, we can solve all the equations in coordinates of Section 1 via the transformation $\partial/\partial s^* = (L_0/L(t)) \partial/\partial s$, i.e., by scaling all differentiation and integration operations appropriately.

We note that a similar reparameterization algorithm was employed in [20, Sec. 2.5] to model polymerization. However, in that work, the authors used the chain rule to write

$$\partial_t \mathbb{X} = \partial_t \mathbb{X}|_{s^*} + s \frac{L'(t)}{L(t)} \partial_s \mathbb{X}, \quad (\text{S21})$$

so that the first term can be obtained using an inextensible algorithm, and the second term added on afterwards. We found this formulation to be highly unstable numerically because each point locally extends in a direction according to its tangent vector. Because of this, numerical instabilities in tangent vector directions tend to be amplified. Our approach is more physical, because it models the addition of monomers at the $s = L$ end, which happens along the direction corresponding to the last tangent vector. As (S21) suggests, we also first solve the equations of Section 1 to evolve the filament positions (inextensible in the s^* coordinate frame), then add the polymerization at the end of the time step.

1.4 Parameters

Throughout this study, we use the parameters in Table 1.

Parameter	Definition	Value	Notes/Reference
κ	Filament bending modulus	0.068 pN· μm^2	Bend persistence length = 17 μm [6]
γ	Filament twist modulus	0.041 pN· μm^2	Twist persistence length = 10 μm [3]
a	Filament radius	4 nm	[7]
L	Filament length	1–2 μm	For nascent filopodia [9]
ℓ_c	Crosslink rest length	100 nm	[15, 16]
K_c	Crosslink stiffness	100 pN/ μm	[15, 16]
N_L	Formin torque	0.1 pN· μm	[10]
μ	Suspending fluid viscosity	1 Pa·s	[11]
$k_B T$	Thermal energy	4.1×10^{-3} pN· μm	
k_{on}	Crosslinker on rate	0.05–0.2 s $^{-1}$	Chosen to give characteristic # of CLs [29]
k_{off}	Crosslinker off rate	2.5–10 s $^{-1}$	
$f_0^{(\text{mot})}$	Motor force magnitude	50 pN/ μm	estimated from the data of [19, 28]
\dot{L}	Actin polymerization rate	0.5 $\mu\text{m}/\text{s}$	Mean value; estimated from [8]
N	Number of tangent vectors	20	
Δt	Time step size	$[5 \times 10^{-5}, 2 \times 10^{-4}]$ s	

Table 1: Parameters for our simulation study.

2 Formin-generated twist and supercoiling

This section provides a linear stability analysis of the behavior that leads to actin supercoiling. Because twist equilibrates much faster than bending, we can say that the twist evolution equation (S4) is in a steady state, so that it obeys the two-point boundary value problem

$$\partial_s^2 \psi = 0 \quad \partial_s \psi(0) = 0 \quad \psi(L) = N_L/\gamma. \quad (\text{S22})$$

This boundary value problem has the obvious solution

$$\psi \equiv \psi(L) = N_L/\gamma, \quad (\text{S23})$$

for the twist profile. The constant twist (S23) implies that the angle of rotation of the fiber $\theta = \int \psi(s) ds = \psi s$, is linear along the fiber.

Armed with this, we can perform a stability analysis on the fiber evolution equation. To do this, we linearize the evolution equation (S2) around a straight fiber $\mathbb{X}_0(s) = (0, 0, s)$, then substitute the constant ψ from (S23). Setting $\mathbb{X} = \mathbb{X}_0 + \delta \mathbb{X}^\perp$, where $\delta \mathbb{X}$ is a *perpendicular* perturbation, we get the linearized dynamics (to first order in δ in the perpendicular direction)

$$\partial_t \mathbb{X}^\perp = \frac{\ln(\epsilon^{-2})}{8\pi\mu} \left(-\kappa \partial_s^4 \mathbb{X}^\perp + \gamma \psi \left(\partial_s \mathbb{X}_0 \times \partial_s^3 \mathbb{X}^\perp \right) \right). \quad (\text{S24})$$

We now follow the technique of [31] by mapping $\mathbb{X}^\perp = (X, Y, \sim)$ to the complex plane, so that the complex number $h = X + iY$ represents the degrees of freedom, and $\partial_s \mathbb{X}_0 \times \partial_s^3 \mathbb{X}^\perp = i \partial_s^3 h$. The transformed evolution equation (S24) becomes

$$\partial_t h = \frac{\ln(\epsilon^{-2})}{8\pi\mu} \left(-\kappa \partial_s^4 h + i \gamma \psi \partial_s^3 h \right). \quad (\text{S25})$$

For linear stability analysis, we set $h(s, t) = e^{\omega t} \xi(s)$, which gives the two point eigenvalue problem

$$\begin{aligned} \omega \xi &= \frac{\ln(\epsilon^{-2})}{8\pi\mu} \left(-\kappa \xi^{(4)} + i \gamma \psi \xi''' \right) \\ \xi''(0, L) &= 0 \quad \xi'''(0, L) = 0. \end{aligned} \quad (\text{S26})$$

Our goal here is to find ψ such that the perturbation is linearly unstable. Similar to [31], we expect that, at the critical $\psi = \psi_{\text{crit}}$, the twisting torque $\sim \gamma \psi$ will be equal to the bending torque $\sim \kappa/L$. As such, we look for a critical value of $\psi_{\text{crit}} = c\kappa/(L\gamma)$ such that there exists an eigenvalue ω in (S26) with positive real part. This can be done numerically using Chebfun [21, 4], an open-source software for numerical computation with functions, which gives

$$\psi_{\text{crit}} \approx 1.41 \frac{2\pi \kappa}{L \gamma}. \quad (\text{S27})$$

Converting this to a number of turns, we find that $N_{t,\text{crit}} = L\psi_{\text{crit}}/(2\pi) = 1.41(\kappa/\gamma)$. For actin filaments, $\kappa \approx 17 \text{ pN}\cdot\mu\text{m}^2$ [6], while $\gamma \approx 10 \text{ pN}\cdot\mu\text{m}^2$ [3]. This gives a critical number of turns $N_{t,\text{crit}} = 2.4$ for actin filaments of given length. If a filament is twisted less than that, it remains straight; if it is twisted more, it supercoils.

A similar stability analysis to the one here was also conducted for a clamped filament being spun at one end [31], and a twisted closed loop [30, 24].

3 Supplemental modeling results

3.1 Motor torque

If the motor action occurs on the fiber boundary rather than the centerline, then motors should exert both a force density $f_{\text{mot}}^{(0)}$ and torque density $n_m = f_{\text{mot}}^{(0)}a$ on the fiber. It is helpful to first consider how the torque by motors changes the profile of twist on the peripheral fibers. When the motors apply a torque along the bottom half of the fiber, they rotate the filament cross section there in the same direction as formin. Fig. S7 shows the effect of this over time; the angle of rotation at the bottom of the filopodium becomes more and more positive, which means the twist becomes more negative, and is no longer constant along the centerline. Thus, while the twist remains positive at the tip in accordance with the boundary condition induced by formin, the effect of the motor torque is to *reduce* the twist along the rest of the filament. Fig. S8 shows that changing the torque induced by formin simply shifts the endpoint/boundary condition for twist at the plus end. Our expectation is therefore that twist from motors will make twist more negative, which will reduce the force driving the fibers inward. This is indeed the case; as shown in Fig. 5B, the amount of compaction in simulations with motor twist is always less than for simulations that do not include motor torque, and the least compact bundle is one with reverse formin twist and CCW motor torque.

3.2 Confining membrane as a cap on outward growth

We mostly simulate the simpler case of the motors acting on the filopodial bundle from a rigid cylindrical filopodial sheath. Here we consider, approximately, the case of deformable membrane by following the formalism in [23]. The mechanical energy of the cylindrical membrane envelope around the filopodial bundle (of radius R and length L) is equal to $E = L[(\pi\kappa/R) + 2\pi\gamma R]$. Here κ is the membrane rigidity ($\kappa \sim 10k_BT$), and γ is the membrane tension ($\gamma \sim 0.001k_BT/\text{nm}^2$).

This energy reaches minimum at given L for radius $R_0 = \sqrt{\kappa/2\gamma} \sim 100$ nm. At this radius, the cylindrical walls of the membrane do not exert any inward force on the actin bundle. Also, the absence of buckling by the membrane (which tries to decrease L and therefore exerts some potentially buckling force) was shown in [23]. Let us consider the case when the radius is greater than R_0 . Then, approximately, the bending term in the membrane energy can be neglected, and the membrane tension is opposed by the elastic force from deforming the 12 outer filaments of the filopodial bundle. By the Laplace Law, the effective outward pressure from the filament bundle onto the circumference of the membrane cylinder, per unit length of the membrane cylinder, is equal to $P = \gamma/R$. Thus, the force per filament, per unit length of the filament, is $f = 2\pi RP/12 \sim \gamma/2 \sim 0.0005k_B T/\text{nm}^2 \sim 1\text{pN}/\mu\text{m}$. Computing the force accurately requires numerically minimizing the elastic energy of the bundle together with mechanical energy of the membrane, but these are very involved numerical calculations [23], so here we limit the analysis to using an approximate constant restraining force from the membrane.

Therefore, to simulate membrane confinement, we add a force proportional to the inward normal vector at each filament point $\mathbf{n}(s) = (-\cos(\theta(s)), -\sin(\theta(s)), 0)$ in the region where the motors act (the outer 1/4 of the filopodium, defined by the initial configuration; see Section 2 for the definition of $\theta(s)$). This corresponds to any radial coordinates exceeding 225 nm. In Fig. S9, we show the results of simulations with membrane force, in particular the endpoint positions of the peripheral filaments, projected onto the xy plane in the same way as Fig. 5A. We observe significantly more compaction when the confinement force is included, regardless of the value of formin torque. Interestingly, simulations with no formin torque or reverse formin torque show that the endpoints form a tight circle of radius approximately 225 nm (which is the beginning of the confining region), which suggests that membrane forces in this case provide a “ceiling” on the expansion of the bundle. By contrast, when formin torque is in the same direction as motors, the synergistic effect is again observed, and the endpoints position themselves anywhere from 0 to 0.2 in radial coordinates. We quantify this by adding to Fig. 5B the mean outer radius when membrane forces are included (yellow circles on the plot). There we see that, even with the extra confinement, the radial coordinates with formin torque in the proper direction are still about 30% lower than those with no formin torque or formin torque in the reverse direction. Thus the synergistic effect of formin and motors is still present, but reduced by the membrane providing a cap on outward displacement.

3.3 Role of transient cross linking and variable growth rates

To study the effect of cross-linking and growth rates, we perform the same sets of simulations as in Section 3.3.3 (i.e., with motor and formin torque), but with the polymerization rate four times more variable (standard deviation $0.2 \mu\text{m/s}$) or the crosslink dynamics four times as slow ($k_{\text{on}} = 0.05/\text{s}$, $k_{\text{off}} = 2.5/\text{s}$). Unlike in simulations with five fibers, here we expect the location of a fiber (in terms of which ring it sits in) to be important for determining the statistics of its motion (since, e.g., motors can only act along the outer 25% of the bundle, which means they can only act along the outer circle of fibers initially). In Figs. S10–S12, we therefore segregate our statistics by ring or circle, showing the central fiber in blue, the smaller circle of 3 fibers in red, the middle circle of 6 fibers in yellow, and the largest outer circle of 12 fibers in purple.

Our first observation is in Fig. S10, where we show the number of rotations each circle of fibers makes around the central fiber in simulations that include (left) formin twist and simulations that do not (right). We see little change in the trajectory of the *midpoints* in this case, but a significant increase in the number of rotations the *inner circle endpoints* make around the central fiber. The increase in rotation comes from the tightening of the bundle in the formin twist case. When the bundle is tighter at the top, more crosslinks can bind the top halves of interior fibers to the rotating outer fibers, increasing the overall rotation of the inner ring. Indeed, the average number of crosslinks is increased by roughly 20% (from 45.3 ± 0.3 to 52.2 ± 0.1) when we account for formin twist.

Similar to the five-filament bundle, we find that increasing the variance in the fiber growth rate or making the crosslink dynamics slower both lead to increased buckling in fiber positions. To demonstrate this quantitatively, we perform a set of simulations with motor and formin torque, but increase the polymerization rate variance from 0.05 to 0.2 (for more variable growth rate), or decrease the crosslink on and off rates by a factor of 4 (to $k_{\text{on}} = 0.05/\text{s}$ and $k_{\text{off}} = 2.5/\text{s}$). In Fig. S11, we plot the mean L^2 curvature and z coordinate of each circle of filaments. We find that, while the trajectories of the outer filaments are dominated by the motors and therefore do not change substantially, the inner filaments tend to buckle more under variable growth rates and more permanent crosslinks, in accordance with our observations in Section 3.1. We also find a correlation between buckling and compaction, as might be expected from the five-filament visual in Fig. 2A: the mean radius of the outer filaments is 0.29 ± 0.01 for the base parameters, 0.32 ± 0.06 for the more variable growth rate, and 0.38 ± 0.05 for the slower CLs. We found that the relationship

between crosslinking and compaction is non-monotonic: if there are no crosslinks, the compaction is 0.44 ± 0.01 , which is less compact than both the base parameter value and the value for longer crosslink residence times.

Movie legends: Movies of 22-filament bundles with and without motor and twisting activity, showing that motors and twist synergize to generate a compact bundle. Crosslinks are shown in yellow, filaments in white, and formins in magenta. The green dots show the clamped ends, which represent the branched actin network beneath the filopodium. The left side of the movie shows a side view, while the right side shows a top view (in this case, the filaments appear to move outward because of the perspective of the observer).

Movie 1: CCW Motors and CCW formin twisting.

Movie 2: No motors, but CCW formin twisting.

Movie 3: CCW Motors, but no formin twisting.

Movie 4: CCW Motors, with CW formin twisting (opposite direction).

References

- [1] David F Anderson. A modified next reaction method for simulating chemical systems with time dependent propensities and delays. *The Journal of chemical physics*, 127(21):214107, 2007.
- [2] Miklós Bergou, Max Wardetzky, Stephen Robinson, Basile Audoly, and Eitan Grinspun. Discrete elastic rods. In *ACM SIGGRAPH 2008 papers*, pages 1–12. 2008.
- [3] Jeffrey P Bibeau, Nandan G Pandit, Shawn Gray, Nooshin Shatery Nejad, Charles V Sindelar, Wenxiang Cao, and Enrique M De La Cruz. Twist response of actin filaments. *Proceedings of the National Academy of Sciences*, 120(4):e2208536120, 2023.
- [4] Tobin A Driscoll, Nicholas Hale, and Lloyd N Trefethen. Chebfun guide, 2014.
- [5] Daniel T Gillespie. Stochastic simulation of chemical kinetics. *Annu. Rev. Phys. Chem.*, 58:35–55, 2007.
- [6] Frederick Gittes, Brian Mickey, Jilda Nettleton, and Jonathon Howard. Flexural rigidity of microtubules and actin filaments measured from thermal fluctuations in shape. *The Journal of cell biology*, 120(4):923–934, 1993.
- [7] Enrico Grazi. What is the diameter of the actin filament? *FEBS letters*, 405(3):249–252, 1997.
- [8] Yueheng Lan and Garegin A Papoian. The stochastic dynamics of filopodial growth. *Biophys. J.*, 94(10):3839–3852, May 2008.
- [9] Natascha Leijnse, Younes Farhangi Barooji, Mohammad Reza Arastoo, Stine Lauritzen Sønder, Bram Verhagen, Lena Wullkopf, Janine Terra Erler, Szabolcs Semsey, Jesper Nylandsted, Lene Broeng Oddershede, Amin Doostmohammadi, and Poul Martin Bendix. Filopodia rotate and coil by actively generating twist in their actin shaft. *Nat. Commun.*, 13(1):1636, March 2022.
- [10] Xi Li and Bin Chen. How torque on formins is relaxed strongly affects cellular swirling. *Biophysical Journal*, 121(15):2952–2961, 2022.
- [11] Katherine Luby-Phelps. Cytoarchitecture and physical properties of cytoplasm: volume, viscosity, diffusion, intracellular surface area. In *International review of cytology*, volume 192, pages 189–221. Elsevier, 1999.

- [12] Yi Man, William Page, Robert J Poole, and Eric Lauga. Bundling of elastic filaments induced by hydrodynamic interactions. *Physical Review Fluids*, 2(12):123101, 2017.
- [13] Ondrej Maxian. *Hydrodynamics of Transiently Cross-Linked Actin Networks: Theory, Numerics, and Emergent Behaviors*. PhD thesis, New York University, 2023.
- [14] Ondrej Maxian. *Hydrodynamics of transiently cross-linked actin networks: theory, numerics, and emergent behaviors*. PhD thesis, New York University, 2023.
- [15] Ondrej Maxian, Aleksandar Donev, and Alex Mogilner. Interplay between brownian motion and cross-linking controls bundling dynamics in actin networks. *Biophysical journal*, 121(7):1230–1245, 2022.
- [16] Ondrej Maxian, Raul P Peláez, Alex Mogilner, and Aleksandar Donev. Simulations of dynamically cross-linked actin networks: morphology, rheology, and hydrodynamic interactions. *PLOS Computational Biology*, 17(12):e1009240, 2021.
- [17] Ondrej Maxian, Brennan Sprinkle, and Aleksandar Donev. Bending fluctuations in semiflexible, inextensible, slender filaments in stokes flow: towards a spectral discretization. *arXiv preprint arXiv:2301.11123*, 2023.
- [18] Ondrej Maxian, Brennan Sprinkle, Charles S Peskin, and Aleksandar Donev. Hydrodynamics of a twisting, bending, inextensible fiber in stokes flow. *Physical Review Fluids*, 7(7):074101, 2022.
- [19] K E Miller and M P Sheetz. Characterization of myosin V binding to brain vesicles. *J. Biol. Chem.*, 275(4):2598–2606, January 2000.
- [20] Ehssan Nazockdast, Abtin Rahimian, Denis Zorin, and Michael Shelley. A fast platform for simulating semi-flexible fiber suspensions applied to cell mechanics. *J. Comput. Phys.*, 329:173–209, 2017.
- [21] Rodrigo B Platte and Lloyd N Trefethen. Chebfun: a new kind of numerical computing. In *Progress in industrial mathematics at ECMI 2008*, pages 69–87. Springer, 2010.
- [22] Thomas R Powers. Dynamics of filaments and membranes in a viscous fluid. *Reviews of Modern Physics*, 82(2):1607F–1615, 2010.

- [23] Sander Pronk, Phillip L Geissler, and Daniel A Fletcher. Limits of filopodium stability. *Phys. Rev. Lett.*, 100(25):258102, June 2008.
- [24] T Sanchez, IM Kulic, and Z Dogic. Circularization, photomechanical switching, and a supercoiling transition of actin filaments. *Physical review letters*, 104(9):098103, 2010.
- [25] Tom Shemesh, Takanori Otomo, Michael K Rosen, Alexander D Bershadsky, and Michael M Kozlov. A novel mechanism of actin filament processive capping by formin: solution of the rotation paradox. *The Journal of cell biology*, 170(6):889–893, 2005.
- [26] Brennan Sprinkle, Ernest B Van Der Wee, Yixiang Luo, Michelle M Driscoll, and Aleksandar Donev. Driven dynamics in dense suspensions of microrollers. *Soft Matter*, 16(34):7982–8001, 2020.
- [27] Anna-Karin Tornberg and Michael J Shelley. Simulating the dynamics and interactions of flexible fibers in stokes flows. *Journal of Computational Physics*, 196(1):8–40, 2004.
- [28] Sotaro Uemura, Hideo Higuchi, Adrian O Olivares, Enrique M De La Cruz, and Shin’ichi Ishiwata. Mechanochemical coupling of two substeps in a single myosin V motor. *Nat. Struct. Mol. Biol.*, 11(9):877–883, September 2004.
- [29] D H Wachsstock, W H Schwarz, and T D Pollard. Cross-linker dynamics determine the mechanical properties of actin gels. *Biophys. J.*, 66(3):801–809, March 1994.
- [30] Charles W Wolgemuth, Raymond E Goldstein, and Thomas R Powers. Dynamic supercoiling bifurcations of growing elastic filaments. *Physica D: Nonlinear Phenomena*, 190(3-4):266–289, 2004.
- [31] Charles W Wolgemuth, Thomas R Powers, and Raymond E Goldstein. Twirling and whirling: Viscous dynamics of rotating elastic filaments. *Physical Review Letters*, 84(7):1623, 2000.

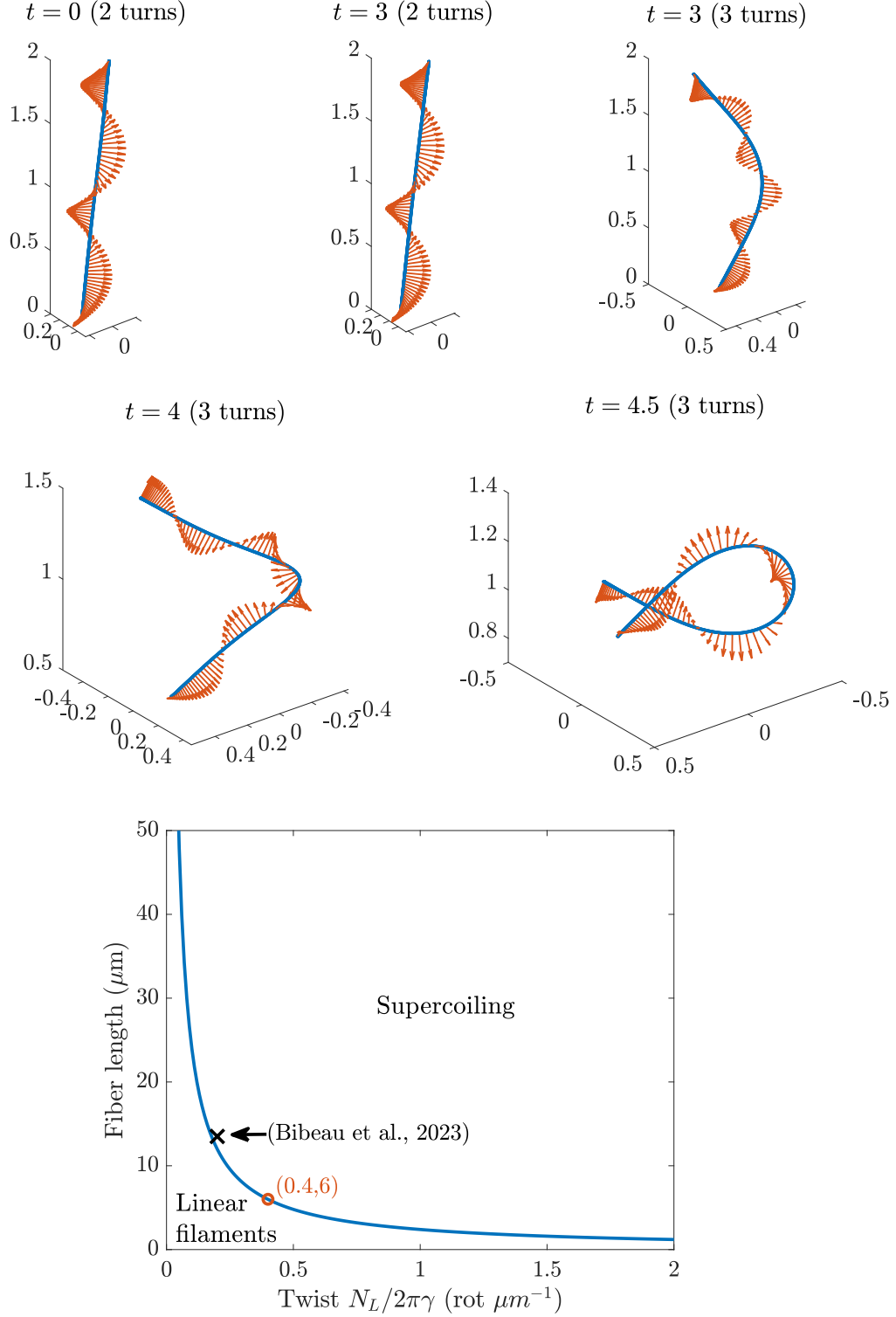


Figure S1: Supercoiled actin filaments. Top plot: behavior of perturbed filaments for 2 absolute twisted rotations (relaxing to straight) and 3 rotations (supercoiling). Bottom: Phase diagram for supercoiling as a function of the fiber length L and twist. For comparison, we plot the data from [3], where the supercoiling threshold was estimated at roughly 0.2 rotations per micron with filaments of length 7–20 μm (for small applied forces).

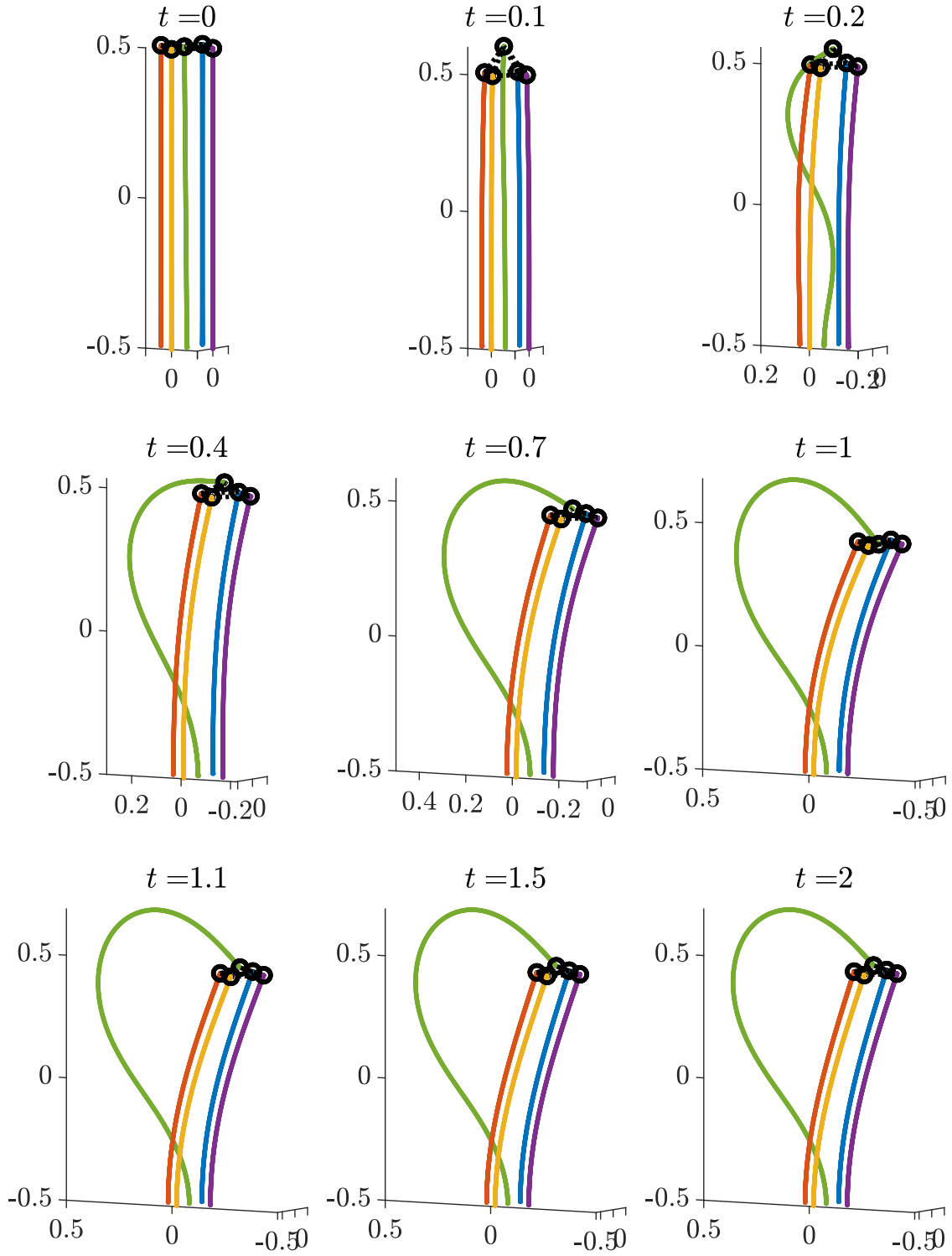


Figure S2: Initial simulation of fiber buckling with polymerization and permanent crosslinking at filament tips. The central filament polymerizes with rate $1 \mu\text{m/s}$ on $0 \leq t \leq 1$ s, after which the configuration relaxes.

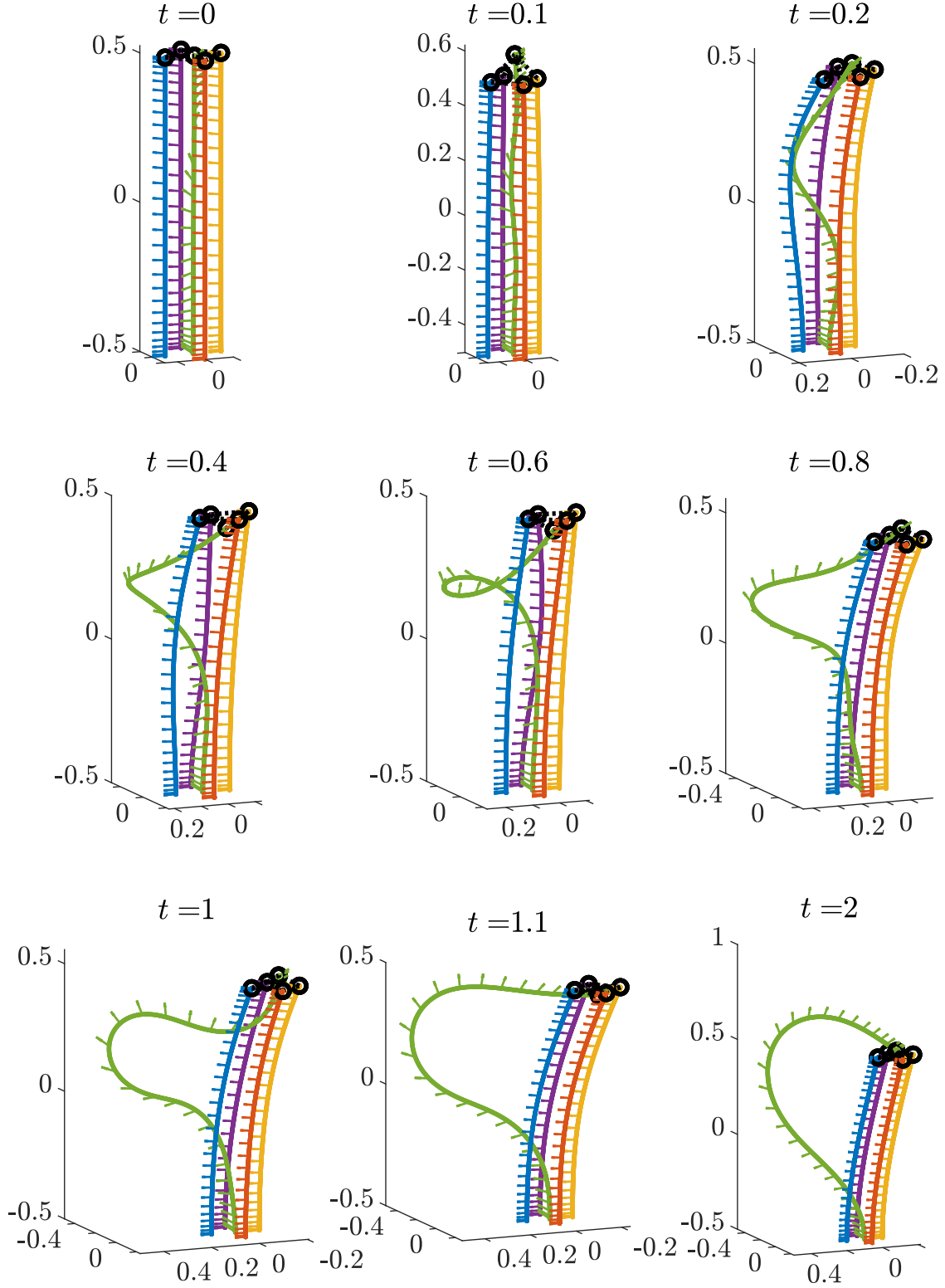


Figure S3: Buckling in a bundle due to polymerization, but with added twist along the fiber centerline using the (unrealistic) torque $N_L = 0.5 \text{ pN} \cdot \mu\text{m}$. Polymerization occurs only for the middle green filament, with $\dot{L} = 1 \text{ } \mu\text{m/s}$ on $0 \leq t \leq 1 \text{ s}$. Arrows show the material frame vectors. Based on our linear stability analysis, we expect supercoiling when the filament length reaches $\approx 1.2 \text{ } \mu\text{m}$.

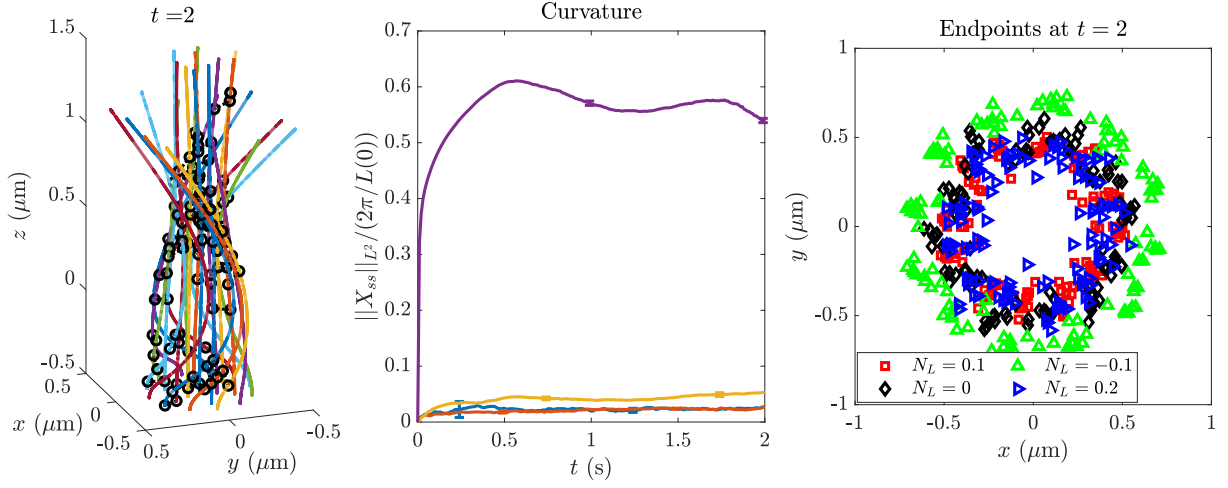


Figure S4: Effect of decreasing the range of motor activity to the lower quarter ($c_m = 1/4$, from $c_m = 1/2$) and the outer $1/8$ (from $1/4$) of the filopodium. Left panel: a snapshot of the filopodium at $t = 1$. Middle panel: the mean curvature on each of the four rings of filaments. Right panel: the endpoint positions at $t = 2$ with different values of the formin torque in $\text{pN} \cdot \mu\text{m}$ (similar to Fig. 5A).

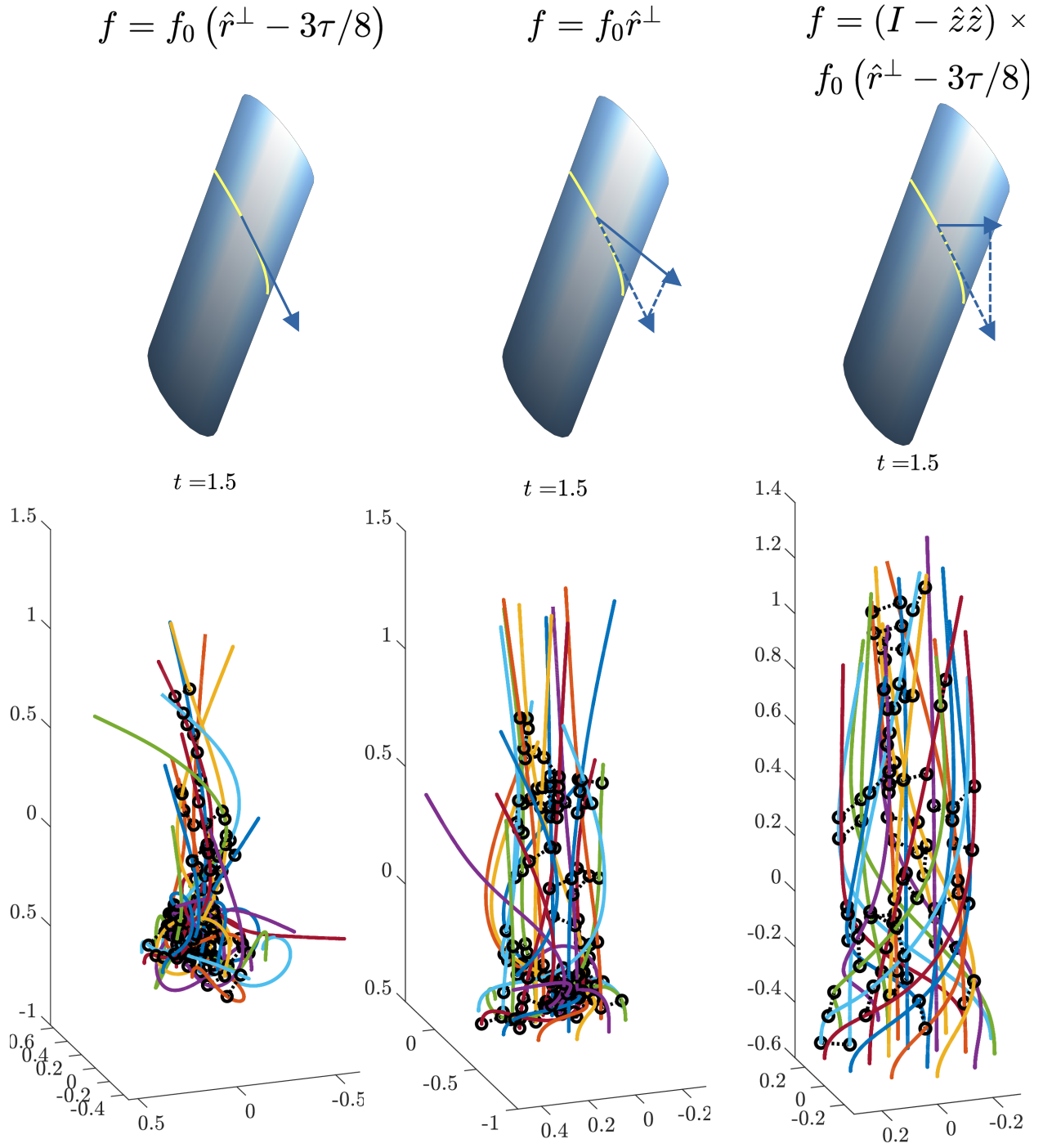


Figure S5: More detailed model of motor forces and resulting simulations. Top panel: defining the directions. The filament is shown as a blue cylinder, with the helical groove (where motors act) in yellow. The corresponding forces can be along both the normal and compressive directions (left), normal direction only (middle), or normal and compressive with downward force projected off (right). Bottom panel: simulation results (configurations at $t = 1.5$ s) considering these three different force models.

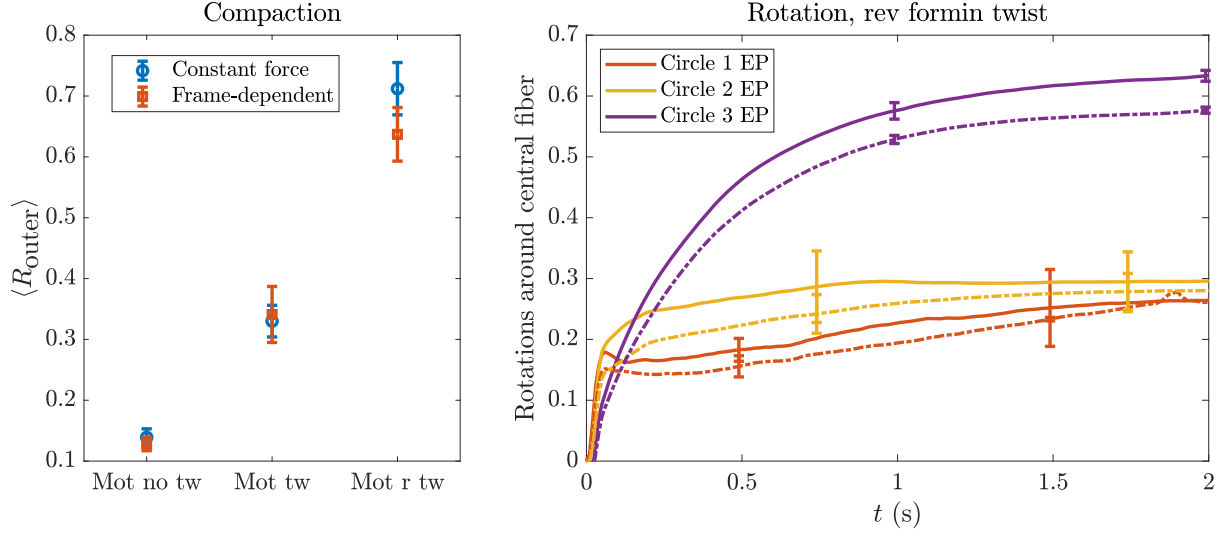


Figure S6: Statistics for simulations with fiber-orientation-dependent (or frame-dependent) forcing, as in the rightmost plot in Fig. S5. The left panel shows the compaction for simulations with CCW formin twist (left), no formin twist (middle), and CW formin twist (right), comparing our default simulations with constant forcing to the simulations with frame-dependent forcing. The rightmost plot shows the most significant difference between the two (reverse formin twist), where we see less rotation of the outer fibers when the force is frame-dependent (dotted lines) vs. when it is constant in time (solid lines).

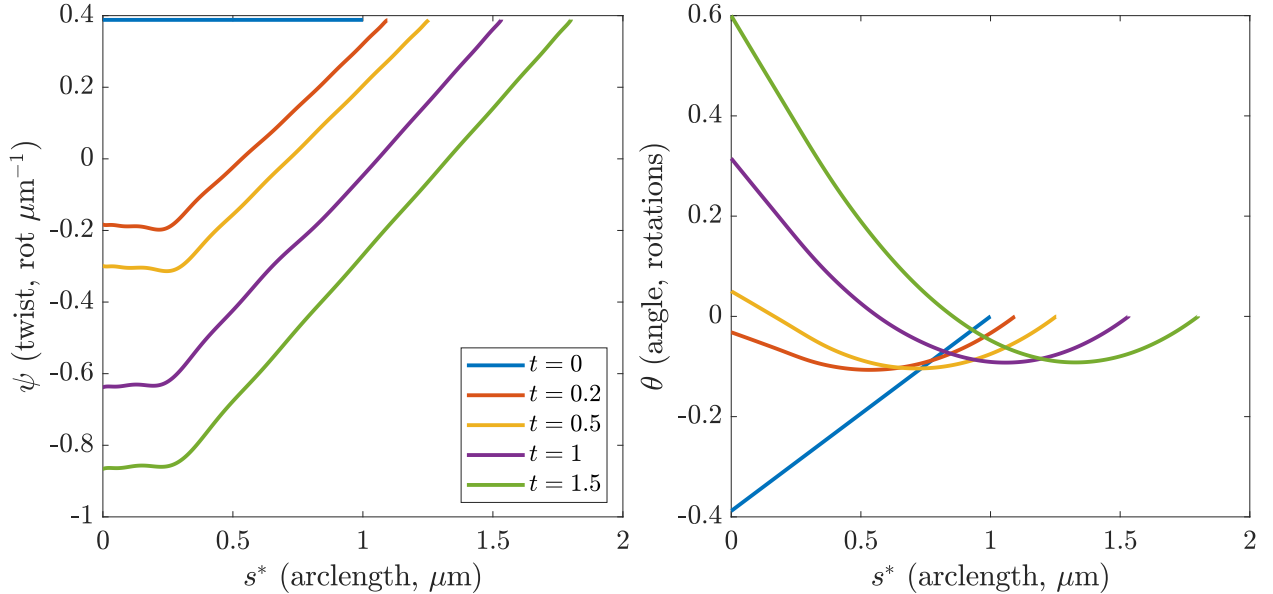


Figure S7: Twist (left, in rotations per μm) and angle of rotation (right, in rotations relative to the endpoint) over time on an outer fiber in the 22-filament bundle. This simulation has a formin torque $N_L = 0.1 \text{ pN}\cdot\mu\text{m}$ and motor torque density $n_m = 0.2 \text{ pN}$.

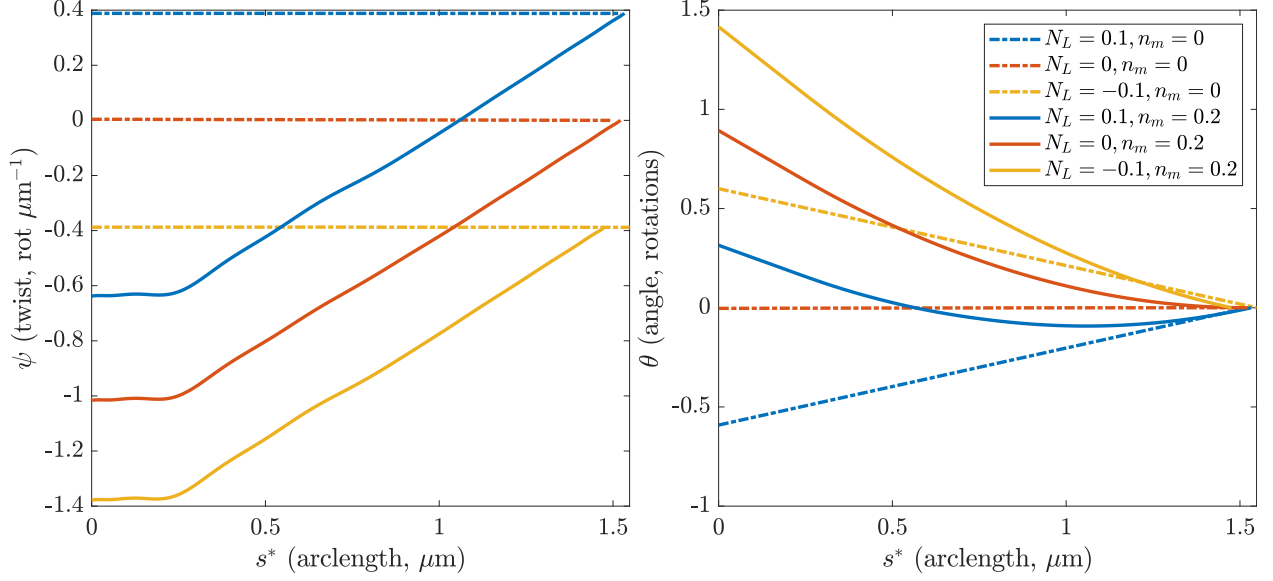


Figure S8: Twist (left, in rotations per μm) and angle of rotation (right, in rotations relative to the endpoint) on an outer fiber in the 22-filament bundle at $t = 1$ s with different parameter values for the formin torque N_L (units $\text{pN}\cdot\mu\text{m}$) and motor torque density n_m (units pN).

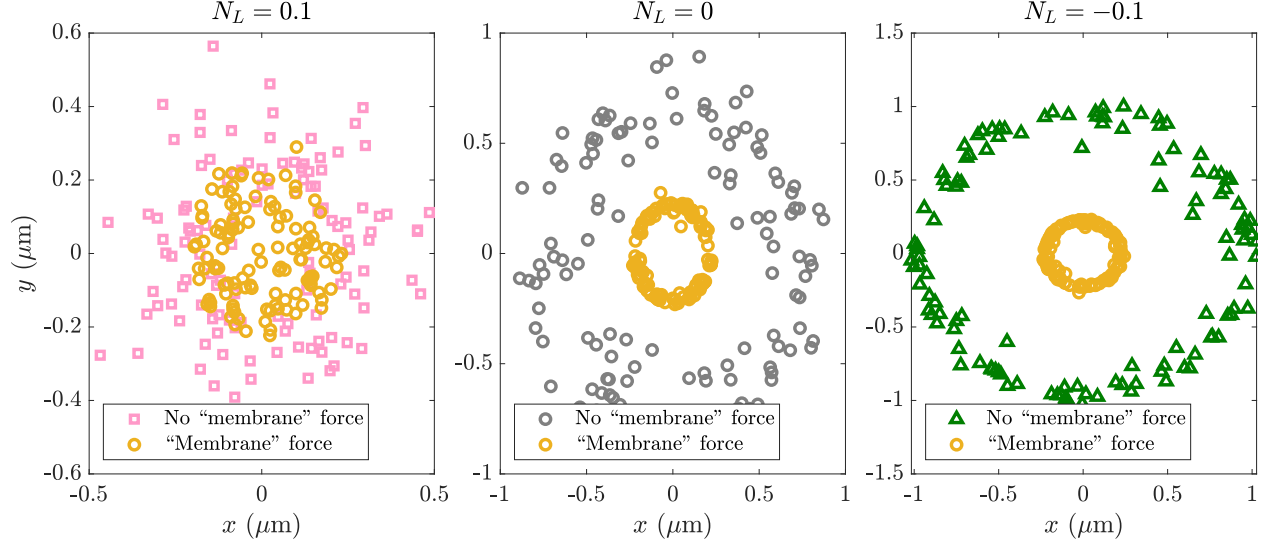


Figure S9: Endpoint position of peripheral filaments with membrane confinement. We show sets of simulations with motor force and torque and varying values of the formin twist, according to the title (units $\text{pN}\cdot\mu\text{m}$). In each case, we project the endpoints of the peripheral filaments onto the xy plane, exactly as in Fig. 5A. In each plot, the yellow circles are simulations with confining force (intended to model the membrane), and the symbols of other colors are simulations without the confining force.

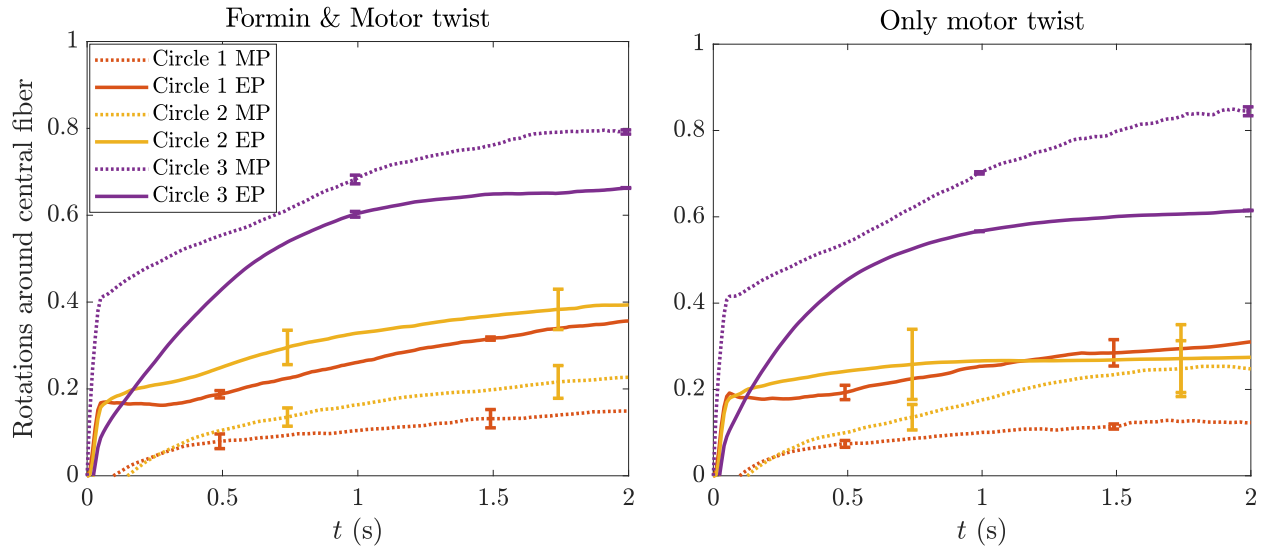


Figure S10: Number of rotations of each circle of filaments around the central filament in the 22-filament bundle. Simulations at left include motor force and torque, as well as formin torque, while simulations at right do not include formin torque. MP = midpoint, EP = endpoint.

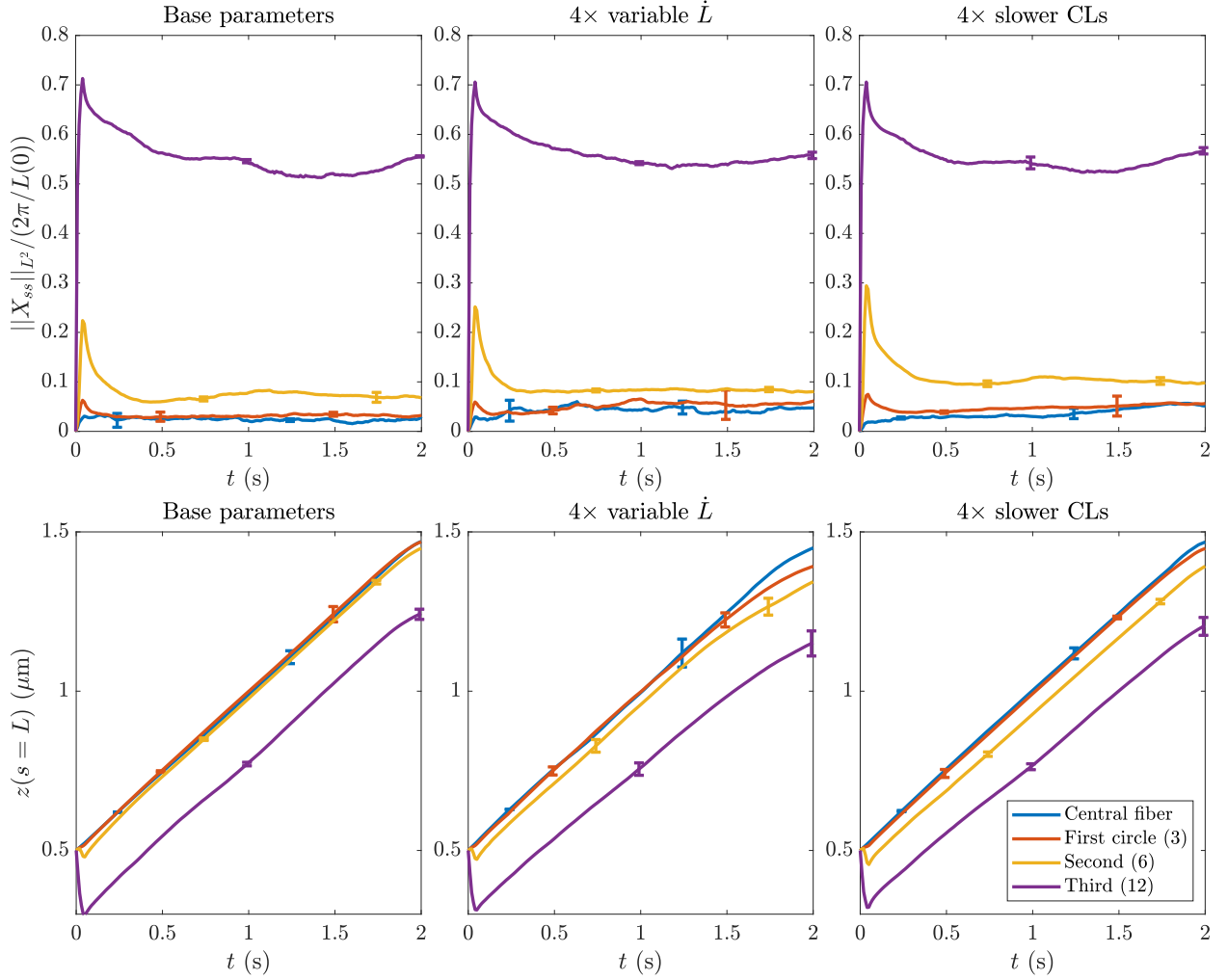


Figure S11: Bending of filaments in 22-filament bundle as a function of polymerization rate variance and cross linking rate. Top: Mean L^2 curvature of filaments, normalized by the curvature of a circle with the same circumference. Bottom: endpoint z coordinate over time. Each statistic is reported by “circle” in the bundle; blue represents the central filament, red the next circle out (3 fibers), yellow the following circle outwards (6 fibers), and purple the outermost circle (12 fibers). The outer circle has high curvature and smaller z coordinate because of motor action. From left to right, we show results for simulations with the base parameters (with motor and formin twisting), a four times larger standard deviation in the polymerization rate, and four times smaller on/off rates for the CLs.

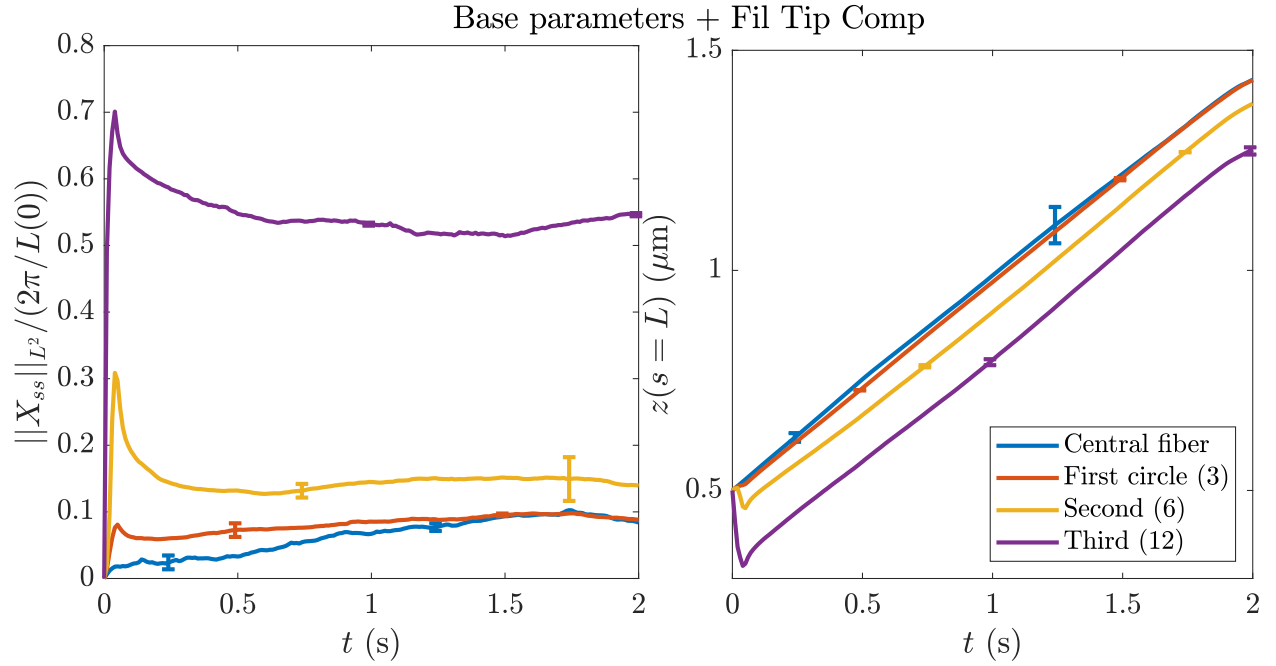


Figure S12: Bending of filaments in 22-filament bundle with the filopodial tip complex. Left: Mean L^2 curvature of filaments, normalized by the curvature of a circle with the same circumference. Right: endpoint z coordinate over time. Compared to the base parameters (left column in Fig. S11), there is more curvature and buckling with the tip complex.